INFLUENCE OF MESH QUALITY AND TURBULENCE MODEL ON COMPUTATION OF TWO-DIMENSIONAL FLOW ON A BIRADIAL TURBINE VOLUTE

Luís Morão Cabral Ferro, lferro@ufersa.edu.br[1,2]
Diogo Neves Ferreira, nevesferreira@tecnico.ulisboa.pt[2,3,4]
Luís Manuel Carvalho Gato, luis.gato@tecnico.ulisboa.pt[2,3]

[1]Universidade Federal Rural do Semi-Árido, RN, Brazil
[2]Instituto Superior Técnico, Universidade de Lisboa, Portugal
[3]IDMEC, Instituto Superior Técnico, Universidade de Lisboa, Portugal
[4]OKEANOS, Centre for Research and Development at University of the Azores, Azores, Portugal

Abstract: The biradial turbine was proposed to equip wave energy power plants with bidirectional air flows. The turbine is symmetrical to a plane perpendicular to the turbine axis, having one volute upstream and another downstream of the rotor. The upstream volute flow is inwards, whereas the flow through the volute downstream of rotor flow is outwards. The volute has a logarithmic spiral shape. Computational Fluid Dynamics (CFD) can be used to compute the flow through the volute. Velocity and pressure field computation of a turbulent flow by a CFD code requires the generation of a mesh and specification of a turbulent model. The iterative process development and convergence depend on the mesh quality and turbulence model. A two-dimensional geometry was used to analyse mesh and turbulence model influence. The mesh was generated by HEXPRESS™ program of NUMECA software. The initial mesh was generated by specifying cell numbers in radial and tangential directions, using the smaller number for the maximum number of refinements for which HEXPRESS™ was able to generate the mesh. For the viscous layer, a stretching ratio equal to 1.2 was specified. The number of layers was the optimal suggested by the program for a y+ equal to one. Next, the mesh was generated multiplying by 1.5 the initial number of cells in radial and tangential directions of the previous mesh. Eight different meshes were generated. Eight turbulent models were compared. Six linear eddy viscosity models: SARC, Spalart-Allmaras, $k - \epsilon$ with extended wall functions (EWF), Realizable $k - \epsilon$ without and with EWF and $k - \omega$ (SST) and two non-linear eddy viscosity models: the Explicit Algebraic Reynolds Stress Model with and without EWF. The quality of all meshes is analyzed by comparing values of mesh quality parameters. Results are presented for the dependence on mesh discretization of mean radial, tangential velocity components, mean velocity angle at outlet section, total pressure loss coefficient and error extrapolation for the more refined mesh. Residuals of the iterative procedure for continuity, momentum equation, and turbulence quantities for the more refined meshes are also shown. Isolines for radial and tangential velocities components using $k - \omega$ are shown. When comparing the evolution of quality parameters with mesh refinement, its quality is always improving. The results show that linear turbulent models are more stable than non-linear ones. The $k - \omega$ and Realizable $k - \epsilon$ were the only ones in which convergence was achieved for all the meshes. Turbulence model $k - \omega$ showed to be the more reliable turbulent model.

Keywords: volute, turbine, biradial turbine, CFD, turbulence

1. INTRODUCTION

Word energy strategy is moving towards a reduction of carbon emission. The space occupied by renewable energy has been growing over the last decades. Wave energy is the largest unexploited energy source from the sea (Ocean Energy Europe, 2022). As referred by Ocean Energy Europe (2022) the potential annual global production is 29,500 TWh. Wave energy is clean and has become increasingly important in Europe's policy of reducing carbon emissions. Nevertheless, wave power production technology needs further development to be more competitive (Kitano *et al.*, 2014). Several different energy conversion systems exist. The oscillating water column (OWC) is an important class of these conversion systems. A comprehensive review of OWC and self-rectifying turbines is presented in Falcão and Henriques (2016). In most OWCs, the air flows between the pneumatic chamber and the atmosphere, driving a self-rectifying turbine. The direction of rotation of the turbine rotor remains constant and is independent of the incoming flow direction. A comparative analysis of self-rectifying air turbines is presented in Falcão *et al.* (2018). One of the referred turbines is

the biradial turbine.

The biradial turbine has been studied at Instituto Superior Técnico (IST) of Lisbon University in the last years (Falcão and Gato, 2011). Numerical results with global performance data are shown in Falcão *et al.* (2013b) and experimental results in Falcão *et al.* (2013a). More results from the development of rotor and guide vanes geometries are available in later publications (Maduro *et al.*;2017, Carrelhas *et al.*;2020, Gato *et al.*;2021).

The present paper considers a version of the biradial turbine with two volutes on each side of the rotor whose function is to collect the flow at exit section of the rotor or to guide the flow to inlet section of a centripetal rotor turbomachine while giving the required angular momentum to the flow at the rotor inlet section. A CFD code is used to compute the flow through the volute. A preliminary analysis must be done to examine effect of mesh discretization and quality, and of turbulence model on the numerical results. The study present in this paper is for a centripetal flow on a two-dimensional geometryd due to CPU limitations.

The methodology section of the paper presents the approach used on the volute design in detail. A brief description of chosen turbulence models, as well as mesh generation techniques and quality parameters of a mesh, are presented. Results of quality parameters for eight different meshes, as well as their evolution with mesh refinement, are shown in the paper. The flow at each mesh is computed using eight different turbulence models, six linear eddy viscosity models and two non-linear eddy viscosity models. The mean radial and tangential velocity results at outlet section components are compared for all the meshes and final errors due to the estimated discretisation. Residuals evolution of mass, momentum and turbulence parameter equations for the more refined mesh are presented for four turbulence models.

2. METHODOLOGY

In this section, the methodology used for the definition of the two-dimensional volute geometry, a brief presentation of turbulence models used for computation of flow field through the turbine volute, and a definition of the mesh quality parameters will be presented.

2.1 Geometry Definition

A volute is typically found at the inlet of a radial centripetal turbomachine or the exit of a radial centrifugal turbomachine. In a centrifugal one, like a pump, the volute collects fluid flow at the rotor outlet section, reduces the angular momentum of the fluid and converts kinetic energy into pressure. For a centripetal rotor, as occurs with a hydraulic turbine, the volute directs fluid flow to the inlet section, and usually, pressure energy is converted into kinetic energy.

For a three-dimensional pump volute, Pfleiderer (1960) established the relation between the maximum radius at each cross-section R_b and the flow rate Q, for inviscid and axisymmetric flow, as given by

$$Q\frac{\theta}{2\pi} = \int_{R_\mathrm{a}}^{R_\mathrm{b}} V_t b(r) dr \,, \tag{1}$$

where r is the radial coordinate, θ the circumferential angle, measured as shown at Fig. 1, and V_t the tangential component of velocity vector. For an inviscid, incompressible and irrotational flow the specific angular momentum $M_\mathrm{m} = rV_t$ is constant and the Eq. (1) can be rewritten (Falcão, 2011)
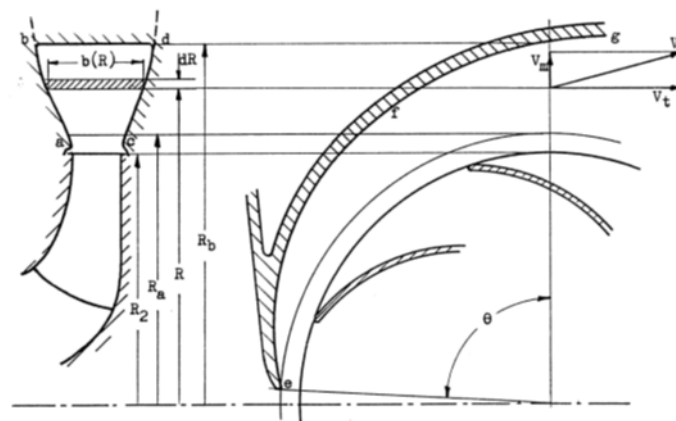

Figure 1: **Spiral volute** (Falcão, 2011)

$$\theta = M_\mathrm{m}\frac{2\pi}{Q} \int_{R_\mathrm{a}}^{R_\mathrm{b}} \frac{b(r)}{r} dr \,, \tag{2}$$

where $b(r)$ is the width of the volute (Fig. 1). The value of R_b can be calculated computing the integral of Eq. (2) using an iterative procedure.

For a two-dimensional flow, the width $b(r)$ is constant, the integral of Eq. (2) has an analytical solution, and the relation between R_b/R_a and the angle θ can be established as:

$$\theta = M_m b(r) \frac{2\pi}{Q} \ln\left(\frac{R_b}{R_a}\right), \tag{3}$$

where $b(r)$ is constant. Rewriting Eq. (3), an explicit relation between R_b and R_a can be defined

$$\ln\left(\frac{R_b}{R_a}\right) = \frac{1}{M_m} \frac{Q}{b} \frac{\theta}{2\pi}. \tag{4}$$

From the definitions of M_m, $Q = 2\pi R_2 b V_r$ and $R_2 = D_2/2$ a new equation for R_b/R_a can be established

$$\ln\left(\frac{R_b}{R_a}\right) = \frac{V_r}{V_t} \theta. \tag{5}$$

The maximum value of R_b/R_a is for $\theta = 2\pi$ and is obtained from Eq. (5)

$$\ln\left(\frac{R_b}{R_a}\right) = 2\pi \frac{V_r}{V_t}. \tag{6}$$

From Eq. (6) a direct relation between the R_b/R_a and angle α is defined as

$$\tan\alpha = \frac{V_r}{V_t} = \frac{1}{2\pi} \ln\left(\frac{R_b}{R_a}\right) \tag{7}$$

The values of angle α for different values of R_b/R_a are presented at Table 1

Table 1: **Variation of angle α with the ratio R_b/R_a.**

R_b/R_a	V_r/V_t	$\alpha(°)$
2	0.1103	6.295
3	0.1748	9.918
4	0.2206	12.442

For the first design of the volute, the radius R_a was assumed constant and equal to $31/30 R_2$ as suggested by Pfleiderer and Petermann (1979). The initially intended shape for R_a versus θ was circumferential. This shape has a constructive impossibility. Due to the thickness of the volute's cross-section normal to the turbine axis, the inlet pipe for a centripetal flow or outlet pipe for a centrifugal one, connecting to the volute, collides with the beginning of the volute. Thus, it becomes necessary to increase the volute radius for $\theta = 2\pi$. The volute shape of the cross-section for the inner radius $r = R_a$ is a logarithmic spiral defined by

$$R_a(\theta) = R_a(\theta = 0)e^{\theta \cot \varphi} \tag{8}$$

The maximum value of R_a, is $R_{a_{max}}$ for $\theta = 2\pi$ and the minimum $R_{a_{min}}$ for $\theta = 0$. The ratio between maximum and minimum values is from Eq. (8)

$$r^* = \frac{R_{a_{max}}}{R_{a_{min}}} = e^{2\pi \cot \varphi} \tag{9}$$

The value of $\cot \varphi$ can be calculated directly from the known value of the ratio r^* and is given by

$$\cot \varphi = \frac{\ln r^*}{2\pi}. \tag{10}$$

The radial coordinates R_a can be computed combining Eqs.(8) and Eq.(10)

$$R_a(\theta) = R_{a_{min}} e^{\theta \frac{\ln r^*}{2\pi}} \tag{11}$$

with θ varying from 0 to 2π. The Cartesian coordinates of inner points can now be easily computed using Eq. (12),

$$\begin{cases} x &= R_a(\theta)\cos\theta \\ y &= R_a(\theta)\sin\theta \end{cases} \tag{12}$$

2.2 Turbulence Models

In this section, a short presentation of used turbulence models is made. The used NUMECA CFD code (NUMECA, 2021) has seventeen turbulence models available. Eight of these were chosen to compute the flow through turbine volute and compare results and iterative convergence. The chosen model was the SARC, the Spalart-Allmaras, the $k - \epsilon$ with EWF, the Realizable $k - \epsilon$ and the Realizable $k - \epsilon$ with EWF, the $k - \omega$ (M-SST), The Explicit Algebraic Reynolds Stress Model (EASRM) S-BSL-EARSM and S-BSL-EARSM with EWF.

The Spalart-Allmaras model (Spalart and Allmaras, 1994) is a one equation model for the turbulent viscosity ν_t. This model is faster and more robust than the standard $k - \epsilon$ (NUMECA, 2021). The SARC model results from a modification of Spalart-Allmaras to include rotation and curvature effects (M L Shur and Spalart, 2000). The $k - \epsilon$ model is a two-equation model, one for the kinetic energy k and the other for the dissipation rate of kinetic energy ϵ which was developed by (Launder and Spalding, 1974). The $k - \epsilon$ with EWF of Hakimi (1997) derives from the low Reynolds $k - \epsilon$ model of Yang and Shih (1993) and as standard $k - \epsilon$ does not solve turbulent equations for k, and ϵ on the first layer of cells close the wall but uses wall functions. Nevertheless, these functions differ from the standard $k - \epsilon$ model of Launder and Spalding (1974).

The Realizable $k - \epsilon$ model with EWF used by NUMECA code was developed by U Goldberg and Chakravarthy (1998). In this model, the k and ϵ equations are not solved at the first layer but defined using wall functions derived from Direct Numerical Simulation (NUMECA, 2021).

The Wilcox $k - \omega$ turbulence model is a two-equations model, k and ω the specific rate of dissipation of k. This model is more robust and accurate than $k - \epsilon$ close the wall but is very sensitive at regions of the fluid where value ω is low (Wasserman,2021;NUMECA,2021). To solve the limitations of original $k - \omega$ model (Menter, 1994) at $k - \omega$ (M-SST) turbulence model combines the original $k - \omega$ model, near the wall, with standard $k - \epsilon$ model, in a $k - \omega$ formulation, in the free-stream (NUMECA, 2021).

As referred by NUMECA (2021) the EARSM can be seen as a subset of non-linear relations in which a part of the higher-order description of physical processes on the Reynolds Stress Model level is transferred into the two-equation modelling level. These models can reproduce the same important physics characteristics of turbulent flows, such as anisotropy, and are much less demanding CPU computer time than the Reynolds Stress Model. One of the models that are available in the NUMECA code is the EARSM model (S-BSL-EARSM) proposed by Langrty and Menter (2009) which is based on the BSL $k - \omega$ model of Menter (1994) with the inclusion of anisotropic effects in the turbulence model.

2.3 Mesh Definition

The meshes were generated by HEXPRESS code of NUMECA. As referred at HEXPRESS™ (2021) the mesh generation process is as follows: import of geometry, creation of initial mesh, adaptation of mesh, snap and optimization of geometry, and insertion of the viscous layer.

The domain geometry is drawn, by SOLIDWORKS, from reading the cartesian point coordinates of boundary curves, usually three curves. As the output of the SOLIDWORKS, a three-dimensional geometry with a constant width is generated and the Parasolid file type is created. This file is the input for the building process of the mesh. The second step is the generation of a coarse hexahedral mesh from the input values of the number of cells in radial, N_r, and tangential, N_t, directions. In the next step, the mesh is adapted to the geometry with successive cell anisotropic subdivisions. At this step, the maximum number of refinements and trimming parameters are specified. In the snap process, the mesh is projected on the geometry. During the optimization phase, the mesh is improved by avoiding, concave and twisted elements and also improving the quality of mesh cells. To finish the mesh it is necessary to generate a boundary layer mesh. The number of layers at the boundary layer was chosen equal to the value suggested as optimum for the HEXPRESS code. To calculate that value it is necessary to specify the value of y^+ for the cell adjacent to the wall as well as the values of reference velocity and length. A value of $y^+ = 1$ was chosen. The value of y_{wall} was computed from Blasius equation (HEXPRESS™, 2021)

$$y_{\text{wall}} = 6 \left(\frac{V_{\text{ref}}}{\nu} \right)^{-\frac{7}{8}} \left(\frac{L_{\text{ref}}}{2} \right)^{\frac{1}{8}} y^+ \tag{13}$$

where V_{ref} and L_{ref}, are the characteristics velocity and length, respectively.

A stretching ratio value σ is needed for the mesh specification in the boundary layer. The parameter σ controls the ratio of the thickness of two adjacent cells (HEXPRESS™, 2021),

$$\sigma = \frac{h_{i+1}}{h_i} \tag{14}$$

where h_i is the cell thickness on a direction normal to the wall. The number of layers and cells inside the boundary layer decreases when stretching ratio values increases. The numerical results may have not accuracy when these values are too small .

Two regions can be distinguished inside a two-dimensional boundary layer, the inner and a outer one (Panton, 2001). The inner region extends to $y/\delta = 0.15$ to $y/\delta = 0.20$ (George,2013; de Brederode, 1997), where $y^+ = u_\tau y/\nu$ and the friction velocity u_τ is defined by

$$u_\tau = \sqrt{\frac{\tau_w}{\rho}} \tag{15}$$

where τ_w is the wall shear stress.

At the inner boundary layer three different zones can be considered (de Brederode, 1997):

- Limiar or laminar sub-layer $0 < y^+ < 5$ within only significant stresses due to viscosity

- Buffer layer $5 < y^+ < 30 - 50$ where coexist viscous and turbulent shear stresses

- Logarithmic zone $y^+ > 50$ within only shear stresses due to turbulence are significant

The number of cells inside each of the three zones above mentioned, N_1, N_2 and N_3, respectively depends on the expansion ratio used on boundary mesh. Values of $N_1 \geq 3$ and $N_3 \geq 6$ are assumed as acceptable (Eça, 2022).

2.4 Mesh quality parameters

Some of the mesh quality criteria that are computed and available in the HEXPRESS quality mesh report are described next. The chosen criteria are the existence of negative, concave, related, or twisted cells, aspect ratio, orthogonality, equiangular skewness, expansion ratio, and adjacent volume.

Negative cells are those with a negative volume. Cells are defined as concave when the Jacobian transformation to a unit cube has at least one zero value for a point located inside of the cell (HEXPRESS™, 2021). Concave and twisted cells are less likely than negative cells to the iterative procedure but the convergence of iterative procedure becomes more difficult and slow. They also should be prohibited because negative cells can appear at the next steps of mesh generation.

Orthogonality is also an important criterion to characterize mesh quality. Consider $\mathbf{e_1}, \mathbf{e_2}, \mathbf{e_3}$ as a unit vector of lines linking the centers of two opposite faces of a hexahedral cell. Compute the three mixed products

$$E_{ijk} = \mathbf{e_i} \cdot (\mathbf{e_j} \times \mathbf{e_k}) \text{ with } \quad i \neq j \neq k \,. \tag{16}$$

The orthogonality is then defined as

$$\text{Orth} = \pi/2 - \arccos(\min E_{ijk}) \,, \tag{17}$$

being $\pi/2$ rad its optimal value.

At FLUENT code (ANSYS, 2016) the orthogonality proprieties are defined otherwise and its definition is also presented here. For a cell is computed the minimum of (Elmekawy, 2018)

$$\frac{\mathbf{A_i} \cdot \mathbf{f_i}}{|\mathbf{A_i}||\mathbf{f_i}|} \quad \text{and} \quad \frac{\mathbf{A_i} \cdot \mathbf{c_i}}{|\mathbf{A_i}||\mathbf{c_i}|} \tag{18}$$

calculated at each face of the cell, where $\mathbf{A_i}$ is the face normal vector, $\mathbf{f_i}$ is the vector from the cell centroid to the center point of the face and $\mathbf{c}$ is a vector connecting the cell centroid and the center of anadjacent cell.

The aspect ratio is also propriety that has to be controlled because may influence the convergence procedure. The aspect ratio AR is defined by Eq. 19

$$AR = \frac{L_{\max}}{L_{\min}}, \tag{19}$$

where $L_{\min}$ and $L_{\max}$ are the shortest and longest cell edge, respectively.

The equiangular skewness is the maximum ratio of the cell's included angle to an equilateral element angle. The equiangular skewness is computed from Eq. 20 applies to all cell types and is available for domains and blocks:

$$\text{Equiangle Skewness} = \max\left(\frac{\theta_{\max} - \theta_e}{\theta_\pi - \theta_e}, \frac{\theta_e - \theta_{\min}}{\theta_e}\right), \tag{20}$$

where $\theta_{\max}$ and $\theta_{\min}$ are the maximum and minimum values of the internal angles of the cell, θ_e the angle of an equiangular element (60 degrees for a triangular face and 90 degrees for a quadrilateral face or hexahedral cell). The best value possible is zero and one the worst.

The mesh expansion ratio is a measured of size variations between two adjacent cells and is defined by Eq.21

$$\text{Expansion ratio} = \max\left(\frac{D_i}{D_j}, \frac{D_j}{D_i}\right), \tag{21}$$
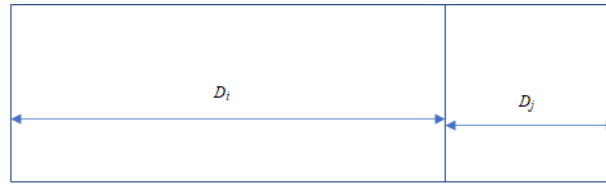
Figure 2: **Definition of mesh expansion ratio.**

where D_i is the distance in one direction, for cell i, between face centres of opposite faces; D_j is the distance in the same direction, between face centres of opposite faces for neighbour cell $i + 1$ as shown at Fig. 2. The maximum values for the three directions is assumed as mesh expansion ratio of cell i.

The last mesh propriety that is going to be mentioned is the adjacent volume ratio, that is the volume jump of a hexahedral cell (HEXPRESS™, 2021) and is defined by Eq. 22:

$$\text{Adjacent Volume cell ratio} = \max\left(\frac{V_i}{V_j}, \frac{V_j}{V_i}\right), \tag{22}$$

where V_i and V_j are the volume of cell i and of a neighbouring cell j.

2.5 Numerical Implementation

The methodology described is going to be used on computation of the centripetal flow through a volute of a biradial turbine. Th rotor has a maximum diameter $D_2 = 1.0$ m. The inlet radius of the volute, R_a, (Fig. 1) varies from 516.7 mm at $\theta = 0$ to 568.3 mm at $\theta = 2\pi$. The minimum and maximum values for outlet radius R_b are 516.7 mm and 1136.7 mm, respectively.

The computational domain must be discretized to compute the inlet flow on the volute (centripetal flow). Computational domain is shown at Fig. 5.

One study objective is to show the influence of mesh discretization on results quality. Eight different meshes were built. A more refined mesh is generated by multiplying by 1.5 the values of N_r and N_t of the coarse mesh. For example from mesh 3 to mesh 4, $N_r = 20 \times 1, 5 = 30$ and $N_t = 120 \times 1, 5 = 180$ (Tab. 2). N_r and N_t are the number of initial cells at radial and tangential directions. $N_i = N_r \times N_t$ in Tab. 2 is the total number of cells at initial mesh. The value of N_r for mesh 1, is the minimum value for which HEXPRESS was able to generate the mesh. The value of N_t for mesh 1 is one for which the mesh had better values of expansion ratio, orthogonality and aspect ratio.

Table 2: **Characterization of final meshes used to compute inlet flow on the volute.**

Mesh	Initial mesh			Number of refinements	B.L. Number of layers	Final mesh	
	N_i	N_r	N_t			Number of cells	Number of nodes
1	11	94	1034	3	16	21372	44422
2	14	120	1680	3	19	26696	55530
3	20	180	3600	3	17	37588	78374
4	30	270	8100	2	18	30253	62886
5	46	405	18360	1	20	27603	56988
6	68	608	41344	1	18	44420	91528
7	103	911	93833	1	16	75119	154262
8	154	1367	210518	1	13	130944	267930

The number of refinements used is the smallest value for which the HEXPRESS code was able to generate each mesh and finish the adaptation, snap and optimization steps. The number of refinements for all the meshes is presented at Tab. 2.

The discretization of boundary conditions results in quality and mesh size. A correct definition of the number of a layer inside the boundary layer mesh is very important. Eight sets of meshes are compared to measure the influence of boundary layer stretching ratio σ on mesh quality., All meshes have N_t=180. The number of initial cells N_r is variable and equal to 12, 18, 24, 30, 36, 42, 48 and 54. At each mesh, the stretching ratio σ varies from 1.1 to 1.7. The optimal number of mesh layers at the normal direction to the wall boundary *NBL* as a function of the stretching ratio *str*, suggested by NUMECA code, is presented in Fig. 3 (a) for all the meshes generated and can be approximate by the power trendline of Eq.23

$$NBL = 35.084\, str^{-2.678} \quad \text{with } R^2 = 0.9151. \tag{23}$$

The number of layers increases quickly when the stretching ratio decreases from 1.2 to 1.1; the total number of cells is multiplicated by approximately 1.25. For *str*=1.1 *NBL* varies from 29 to 36 while for *str*=1.2 *NBL* this variation is from 23

to 29. At Fig. 3 (b) the evolution of maximum expansion ratio value *Mexpr* with stretching ratio, that can be approximated by the equation 24

$$Mexpr = 26.499 \, str^{-3.394} \quad \text{with } R^2 = 0.7447. \tag{24}$$

The quality of the mesh, concerning the expansion ratio, also get worse when the stretching ratio decreases. For a stretching ratio equal to 1.1 the maximum values are between 20.07 and 39.5, with a mean value of 26.5 and a standard deviation of 5.59. The cell number with an expansion ratio greater than 5 is between 181 and 629, with a mean value of 444.6 and a standard deviation of 162.1. When the stretching ratio is equal to 1.2, the maximum values are between 19.87 and 10.45, with a mean value of 13.43 and a standard deviation of 33.12. The number of cells with a value of expansion ratio greater than 5 is between 104 and 3, with a mean value of 13.4 and a standard deviation of 33.1. The mesh quality is much improved when the stretching ratio is increased from 1.1 to 1.2. Meshes with a stretching ratio equal to 1.2 have better quality and are smaller.
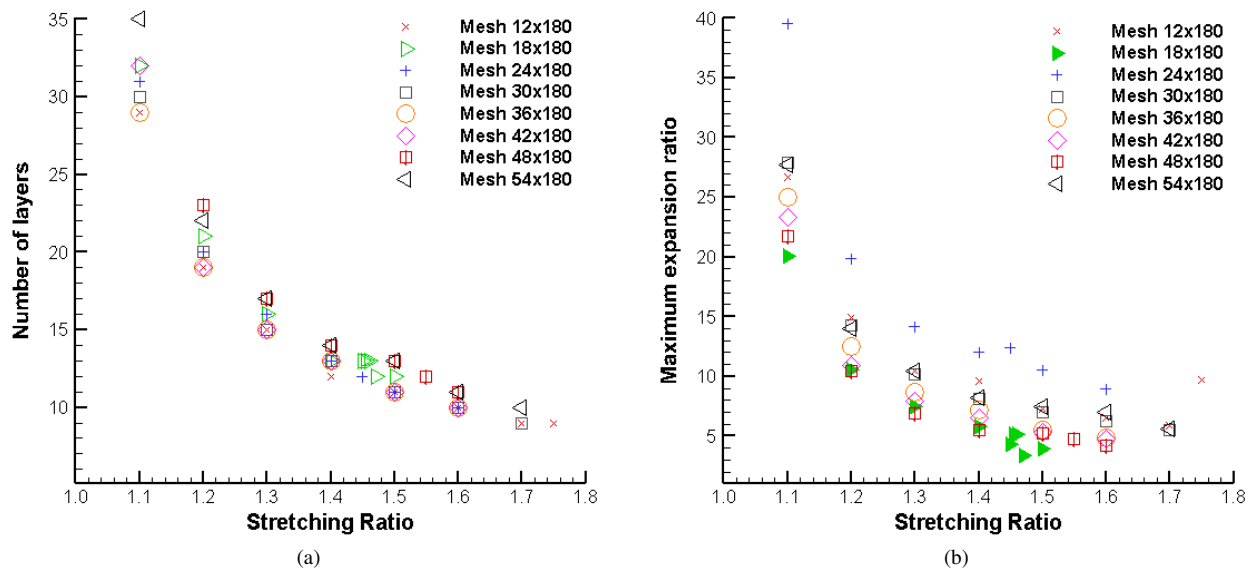

Figure 3: **Influence of stretching value on the mesh: (a) number of optimal layers and (b) maximum values of expansion ratio.**

The number of layers used at discretization of boundary layer must respect the criterion specified at section 2.3 At Fig. 4 it is represented the distribution of cells, on a normal direction to the wall, at the three zones of inner boundary layer zone, N_1, N_2 and N_3, as a function of the stretching ratio. Results presented at Fig. 4 show that only meshes with $str \leq 1.2$ have $N_1 \geq 3$ and with $str \leq 1.4$ have $N_3 \geq 6$.
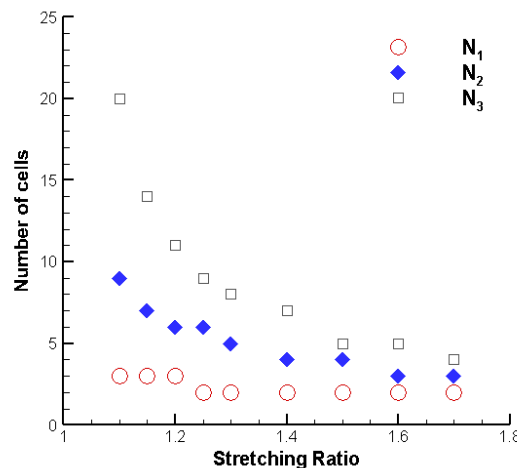

Figure 4: **Variation with stretching ratio of cell number distribution at inner boundary layer zone**.

The computational domain discretized by mesh number 4 is represented at Fig. 5. All meshes generated have the number of layers at BL mesh suggested as optimal by NUMECA. A stretching ratio equal to 1.2 was chosen. The number of refinements used is the lower admissible by HEXPRESS code used to generate the meshes. A complete characterization of all meshes built is presented at Tab. 2.
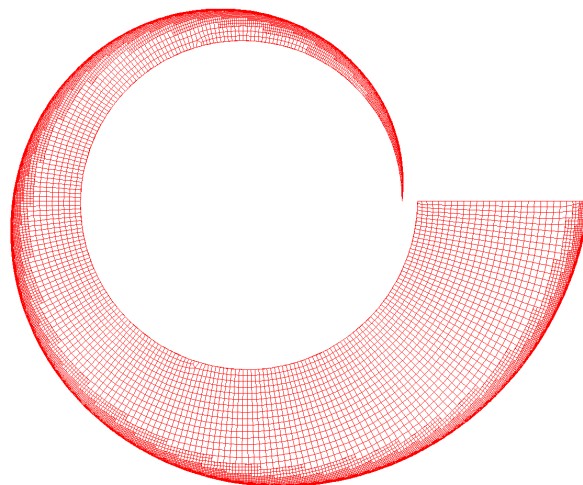

Figure 5: **Computational domain discretized with mesh number 4.**

The first chosen criterion to analyse mesh quality was the mesh expansion ratio, to which NUMECA suggests that the maximum value must not exceed 5.0. Although all the meshes have a cell with an expansion ratio that does not respect the minimum value, the number of cells with an expansion ratio that exceeds 5.0 is very low. The minimum number is 2 and the maximum 20, and its percentage decreases when the mesh is refined from mesh 1 to 8, from 0.0140% to 0.0015. The maximum number of cells in percentage is 0.066%, which indeed is a very low value. The distribution of expansion ratio values for all the meshes is shown at Tab. 3.

Table 3: **Characterization of expansion ratio for all the used meshes.**

Mesh	Maximum value	5-10	10-15	15-20	>20	> 5	
						Number	%
1	14.9701	1	2	0	0	3	0.01404
2	14.3147	1	2	0	0	3	0.01124
3	10.3792	1	2	0	0	3	0.00798
4	10.9510	18	2	0	0	20	0.06611
5	16.6521	1	0	2	0	3	0,01087
6	12.1606	0	2	0	0	2	0.00450
7	12.8402	0	2	0	0	2	0.00266
8	16.0819	0	0	2	0	2	0.00153

At Tab. 4 values of orthogonality for the eight meshes are presented. Following NUMECA recommendation HEX-PRESS™ (2021) the minimum value acceptable is $15°$. Although some cell has a value of orthogonality lower than $15°$ is a number very small compared to the total number of cells (31 is the maximum at mesh 1 and 2), which correspond to a percentage 0.145% at mesh 1. Another criterion referred to at (HEXPRESS™, 2021) is that the average value must be greater than $75°$. The percentage of elements with orthogonality greater than $75°$ increases from $98,11\%$ to 99.64% from mesh 1 to mesh 8, and the average values from $84.00°$ to $86.34°$. The percentage of cells with an orthogonality $\geq 75°$ is almost always increasing when the mesh is refined, and the number with a value lower than $15°$ is always decreasing in

Table 4: **Mesh quality relative to orthogonality in degrees.**

Mesh	Minimum value	0-10°	10-15°	15-30°	30-75°	$\geq 75°$		$< 15°$	
						Number	%	Number	%
1	7.98	20	11	53	344	20968	98.11	31	0.145
2	7.57	20	11	63	376	26244	98.31	31	0.116
3	7.13	17	9	55	396	37133	98.79	26	0.069
4	7.43	21	8	47	346	29835	98.62	29	0.096
5	7.84	22	10	51	317	27211	98.58	32	0.116
6	7.41	21	8	68	307	44040	99.14	29	0.065
7	6.77	21	8	52	376	74678	99.40	29	0.039
8	6.48	15	8	40	342	130478	99.64	23	0.018

percentage and is absolute value also decreases from mesh 1 to mesh 8. The values of orthogonality as recommended by HEXPRESS™ (2021) are always greater than $5°$.

The values of orthogonality as defined by the code FLUENT are presented at Tab. 5. At Elmekawy (2018) is referred that values smaller than 0.001 are unacceptable, between 0.001 and 0.14 are bad, between 0.14 and 0.2 are acceptable, between 0.2 and 0.7 are good, between 0.7 and 0.95 very good and greater than 0.95 excellent. At all meshes do not exist unacceptable cell. The absolute value and percentage of bad cells is very low, (the greatest number of cell is 35 and the lower one 24) and the percentage decreases from 0.112% at mesh 1 to 0.019% at mesh 8. Otherwise the percentage of very good and excellent cells increases, in percentage, from $99,31\%$ to $99,96\%$, almost 100% from mesh 1 to mesh 8. The percentage of excellent cells is also always increasing when the mesh is going to be refined. The lower value from mesh 1 is $92,02\%$ and the bigger value is $97,22\%$ at mesh 8.

Table 5: **Mesh quality relative to orthogonality as defined at FLUENT.**

Mesh	Minimum value	0-0.001	0.001-0.14	0.14-0.2	0.2-0.7	0.7-0.95	0.95-1.0	<0.14	
								Number	%
1	0.11285	0	24	17	106	1559	19666	24	0.112
2	0.92952	0	35	4	41	1923	24663	35	0.131
3	0.93157	0	32	4	51	2607	34838	32	0.085
4	0.93262	0	35	2	45	1921	28199	35	0.116
5	0.92877	0	29	12	42	1263	26193	29	0.105
6	0.93161	0	34	2	54	1705	42565	34	0.077
7	0.93458	0	31	2	58	2668	72316	31	0.041
8	0.93635	0	25	3	29	3584	127254	25	0.019

At Tab. 6 the aspect ratio values for all the meshes are presented. Considering that the unacceptable limit is 1000 (Mayo and Lestriez, 2020) it can be observed that this values do not exists on the meshes generated. Biggest value is 694.3 at mesh 5. The maximum value decreases when mesh is refined and the number of refinements is constant (mesh 1 to 3, three refinements; mesh 4 two refinements and 5 to 8 only one refinement).

Table 6: **Mesh quality relative to aspect ratio.**

Mesh	Maximum value	0-100	100-200	200-300	300-400	400-500	>500	
							Number	%
1	684.3954	20067	1275	13	7	3	7	0.033
2	470.9084	25992	687	8	5	4	0	0.000
3	357.0313	37569	14	3	2	0	0	0.000
4	436.1237	29915	324	6	5	3	0	0.000
5	649.3227	26441	1134	14	5	4	5	0.017
6	342.4074	44251	159	7	3	0	0	0.000
7	313.6606	75099	15	4	1	0	0	0.000
8	204.8632	130934	9	1	0	0	0	0.000

The distribution of equiangular skewness for all the meshes is presented at Tab. 7. According to Elmekawy (2018), values between zero and 0.25 are excellent, between 0.25 and 0.5 are very good, between 0.5 and 0.8 are good, between 0.8 and 0.95 are acceptable, between 0.0.95 and 0.97 are bad and finally greater than 0.97 are unacceptable. All the meshes generated do not have bad or unacceptable elements. The number of excellent elements increase, in percentage, from $97,53\%$ to 99.16% from the mesh 1 to mesh 8. The percentage of very good, good and acceptable cells decrease and has is highest values for the coarse mesh (0.20% for mesh 1 and 0.02% at mesh 8).

Table 7: **Mesh quality relative to equiangular skewness.**

Mesh	Maximum value	0-0.25	0.25-0.5	0.5-0.8	0.8-0.95	0.95-0.97	>0.97	>0.9	
								Number	%
1	0.92812	20837	380	104	43	0	0	40	0.187
2	0.92952	26028	525	102	41	0	0	38	0.142
3	0.93157	36861	582	94	51	0	0	34	0.090
4	0.93262	29592	527	89	45	0	0	36	0.119
5	0.92877	27041	415	105	42	0	0	40	0.145
6	0.93161	43738	530	98	54	0	0	36	0.081
7	0.93458	74189	795	78	58	0	0	33	0.044
8	0.93635	129838	996	81	29	0	0	26	0.020

Values of adjacent volume ratio for all the meshes are presented at Tab. 8. At (POINTWISE, 2021) video it is referred that the maximum value acceptable is around 10. At (SIMSCALE, 2022) a maximum value of 20 is referred and of 10 is recommended. All the meshes respect these criteria as mesh 5 has only two cell with a value smaller than 10.3. The percentage with an adjacent volume ration between one and two, increases from $85,95\%$ at grid 1 to $93,76\%$ at grid 8.

Table 8: **Mesh quality relative to adjacent volume ratio.**

Mesh	Maximum value	1-2	2-4	4-6	6-8	8-10	>10	>5 Number	>5 %
1	8.6741	18369	2454	531	16	2	0	135	0.632
2	8.5252	22984	3125	583	2	2	0	50	0.187
3	7.9672	31905	4517	1158	8	0	0	91	0.242
4	8.3281	26190	3066	875	120	2	0	232	0.767
5	10.2763	25174	2135	290	2	0	2	42	0.152
6	8.3664	40749	3210	459	1151	4	0	36	0.081
7	7.8141	69619	4345	1151	4	0	0	4	0.005
8	9.9042	12274	4658	3260	250	2	0	596	0.455

To compute the centripetal flow through the volute, it is necessary to specify boundary conditions. A three-dimensional domain with constant width must be considered to compute a two-dimensional flow using NUMECA code. At the inlet section, the velocity vector is normal, and the velocity profile must be specified. At the outlet section, the constant average pressure is assumed. At wall surfaces of the volute, a no-slip condition of zero velocity is prescribed. Two mirror surfaces were considered to simulate a two-dimensional.

3. RESULTS

The geometry object of study and numerical computation is a volute of a biradial turbine. As referred, the rotor has a maximum diameter $D_2 = 1.0$ m. The inlet radius R_a varies from 516.7 mm at $\theta = 0°$ to 568.3 mm at $\theta = 360°$. The minimum and maximum values for R_b are 516.7 mm and 1136.7 mm, respectively. The flow assumed as incompressible, is centripetal and the velocity profile at inlet has $\Gamma = rV_t$ constant, with the velocity normal to the inlet section. The values of $|V|$ at $r = 0.568$ m and $r = 1.1367$ m are 7.975 m/s and 7.016 m/s, respectively. At outlet section a constant average pressure boundary condition was prescribed with $p = p_{\text{atm}}$.

The inlet flow through the volute was computed for all the meshes, from mesh 1 to mesh 8. The turbulence models chosen were those referred at section 2.2 For all turbulence models, the Courant-Friedrichs-Lewy (CFL) number was $CFL = 3.0$, with the exception of S-BSL-EARSM and S-BSL-EARSM with EWF, for which only $CFL = 2.0$ convergence was achieved. Only three of these models were able to get convergence with all the meshes: the Spalart-Allmaras, the $k - \epsilon$ with extended wall function and $k - \omega$. For mesh number 5, SARC, Realizable $k - \epsilon$ and the Realizable $k - \epsilon$ with EWF do not achieve convergence. With S-BSL-EARSM turbulence model convergence was not obtained with meshes 6, 7 and 8. Finally, S-BSL-EARSM with extended wall function model does not converge with mesh number 6. The relative error for mass flow is very low, less than 0.1% for all the turbulence models and meshes when a converged result is obtained. Results of mean absolute values of radial and tangential components of velocity, $\bar{V}_r$ and $\bar{V}_t$, and of mean angle $\bar{\alpha}$ at outlet section as well as pressure loss coefficient, K_{volute} defined by Eq. 25.

$$K_{\text{volute}} = \frac{p_{t_{inlet}} - p_{t_{outlet}}}{0.5\rho V_{imed}^2}, \tag{25}$$

where V_{imed} is the mean normal velocity at inlet section, that is equal to $(7.016 + 7.975)/2 = 7.4955$ m/s, are going to be presented.

At Fig. 6 (a) the evolution of computed velocity angles $\bar{\alpha}$ for meshes 2 to 8 with N^*, defined by Eq. 26,

$$N_j^* = \sqrt{\frac{N_i(\text{mesh } 8)}{N_i(\text{mesh} j)}}. \tag{26}$$

are shown for all the referred turbulence models. At Fig. 6 (b) a second degree polynomial regression for results with $k - \omega$ model is shown. At Tab. 9 correlation quadratic functions for all the turbulent models are presented. The correlation factor R^2 is also presented at this table and show very good values for all turbulence models, with exception of S-BSL-EARSM

Table 9: **Correlations of velocity angle $\bar{\alpha}$ for all the turbulence models.**

| Turbulence model Model designation	Number	Quadratic equation of $\bar{\alpha}$	R^2	Error Absolute	Error Rel. (%)
SARC	1	$\alpha = 0.0081(N^*)^2 - 0.3306N^* + 10.0078$	0.9988	0.271	2.7
Spalart-Allmaras	2	$\alpha = 0.0164(N^*)^2 - 0.4539N^* + 10.1905$	0.9693	0.505	4.95
$k - \epsilon$ with EWF	3	$\alpha = 0.0062(N^*)^2 - 0.3249N^* + 9.9293$	0.9822	0.263	2.64
Realizable $k - \epsilon$	4	$\alpha = 0.0160(N^*)^2 - 0.4474N^* + 9.9769$	0.9918	0.385	3.94
Realizable $k - \epsilon$ with EWF	4A	$\alpha = 0.0201(N^*)^2 - 0.4933N^* + 9.8138$	0.9970	0.428	4.36
$k - \omega$	5	$\alpha = 0.0041(N^*)^2 - 0.3092N^* + 9.8521$	0.9858	0.257	2.61
S-BSL-EARSM	6	$\alpha = 0.0225(N^*)^2 - 0.5700N^* + 10.5897$	0.8697	1.475	13.93
S-BSL-EARSM with EWF	7	$\alpha = 0.0219(N^*)^2 - 0.4986N^* + 10.1858$	0.9533	0.542	5.32

(a)

(b)
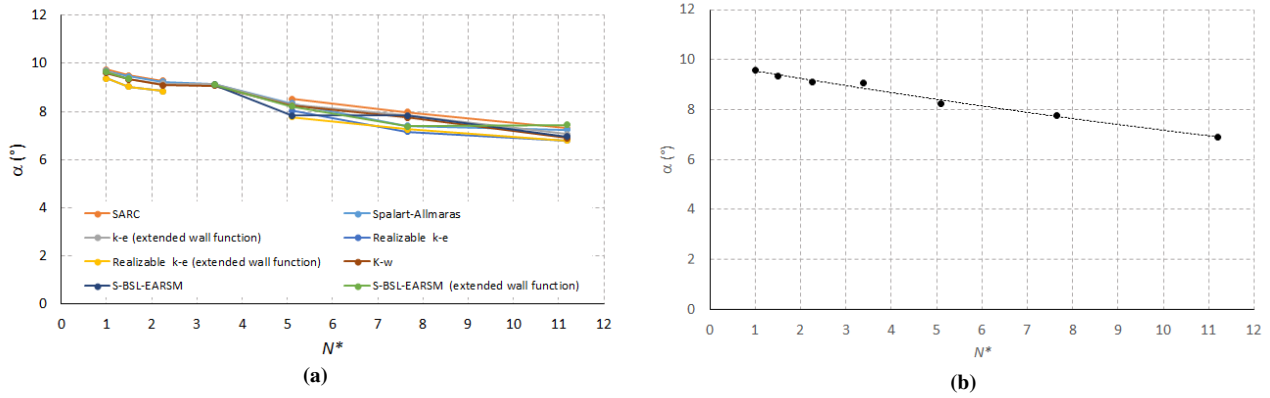
Figure 6: **Mesh discretization and turbulence model influence on velocity angle $\bar{\alpha}$: (a) values for all turbulence models and (b) Polynomial interpolation for $k - \omega$ model.**

model. For this last model convergence was not achieved for meshes 6 to 8 and final results for this model were obtained with a more coarse mesh. The correlation factor for all linear eddy viscosity models (1-5), is greater than 0.98. At the two last columns of this table the absolute and relative error are exhibit. Absolute error is the difference between values computed at the more refined mesh (number 8) and values for a mesh with an infinity number of cells (N^*=0). This value, called exact value, is obtained from the quadratic equations for $\bar{\alpha}$ with $N^* = 0.0$. The relative error is the quotient between absolute error and exact value. SARC, $k - \epsilon$ with EWF and $k - \omega$ presents the lower error, minor than 3%, and the S-B-EARSM models has major errors, (13.93% and 5.32%).

A comparison of evolution of mean tangential velocity component $-\bar{V}_t$ at outlet section with the N^*, is shown at Fig. 7 (a). The correlation for $k - \omega$ turbulence model, is presented at Fig. 7 (b). Equations for quadratic interpolation of mean tangential velocity $\bar{V}_t$ for all the turbulence models are also presented at Tab. 10. R^2 values of the referred correlations and the correspondent absolute and relative errors are also shown. Values of R^2 for $\bar{V}_t$ are between 0.9325 for S-BSL-EARSM to 0.9937 for SARC. The exact values, for N^*=0, excluding S-BSL-EARSM model, are between 7.1613 (S-BSL-EARSM with EWF) and 7.5861 m/s for $k - \omega$ model. Figure 7 (a) also shown that the difference between computed values for the different turbulent model is reduced when the size of meshes increases. As shown at Tab. 10 the
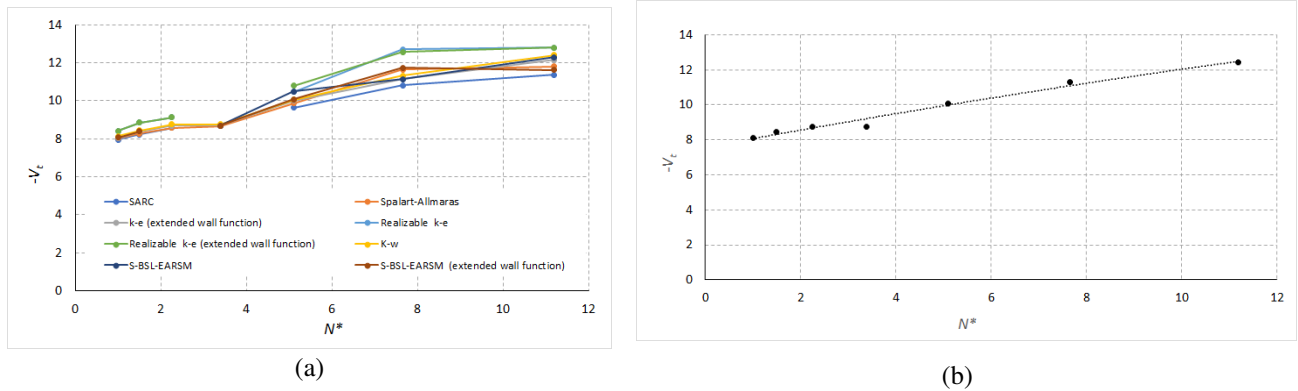

(a)

(b)

Figure 7: **Mesh discretization and turbulence model influence on mean tangential velocity at outlet section $\bar{V}_t$: (a) values for all turbulence models and (b) polynomial interpolation for $k - \omega$ model.**

.

Table 10: **Correlations of tangential velocity component $\bar{V}_t$ for all the turbulence models.**

Turbulence model	Quadratic equation of $-\bar{V}_t$	R^2	Error	
			Absolute	Rel. (%)
1	$V_t = -0.0186(N^*)^2 + 0.5683N^* + 7.3859$	0.9937	0.565	7.66
2	$V_t = -0.0215(N^*)^2 + 0.6718N^* + 7.1731$	0.9499	0.838	11.68
3	$V_t = -0.0081(N^*)^2 + 0.5151N^* + 7.4930$	0.9805	0.537	7.16
4	$V_t = -0.0321(N^*)^2 + 0.8466N^* + 7.5133$	0.9620	0.896	11.93
4A	$V_t = -0.0367(N^*)^2 + 0.8968N^* + 7.4665$	0.9836	0.939	12.58
5	$V_t = -0.0054(N^*)^2 + 0.4992N^* + 7.5861$	0.9813	0.538	7.10
6	$V_t = -0.0470(N^*)^2 + 1.1332N^* + 5.6436$	0.9587	3.042	53.90
7	$V_t = -0.0291(N^*)^2 + 0.7422N^* + 7.1613$	0.9325	0.900	12.57

relative medium error, excluding S-BSL-EARSM model is about 10%, with a maximum of 12.57% for Realizable $k - \epsilon$ model and a minimum of 7.1% for $k - \omega$.

Equations for quadratic interpolation of the symmetric of mean radial velocity $\bar{V}_r$ at outlet section are presented at Tab. 11. The R^2 of $\bar{V}_r$ correlations are between 0.30 and 0.73, which are not good values, probably due to the small variations of the radial component V_r when mesh is refined and also due the position of outlet section to close of the wall for small values of θ. Although the absolute and relative error are very low the maximum and minimum absolute error are 0.101 (S-BSL-EARSM model) and 0.004 (SARC model). The correspondent relative error are 0.101% and 0.26%.

Table 11: **Correlations of radial velocity component $\bar{V}_r$ for all the turbulence models.**

Turbulence model	Quadratic equation of $-\bar{V}_r$	R^2	Error Absolute	Error Rel (%)
1	$V_r = -0.0006(N^*)^2 + 0.0120N^* + 1.3609$	0.7928	0.011	0.78
2	$V_r = -7.0 \times 10^{-5}(N^*)^2 + 0.0048N^* + 1.3757$	0.3698	0.004	0.26
3	$V_r = -9.0 \times 10^{-5}(N^*)^2 + 0.0033N^* + 1.3778$	0.4746	0.005	0.38
4	$V_r = -0.0009(N^*)^2 + 0.0170N^* + 1.3644$	0.6716	0.014	1.02
4A	$V_r = -0.0010(N^*)^2 + 0.0185N^* + 1.362$	0.7328	0.016	1.19
5	$V_r = 0.0000(N^*)^2 + 0.0050N^* + 1.3803$	0.2977	0.006	0.46
6	$V_r = -0.0027(N^*)^2 + 0.0374N^* + 1.5206$	0.8688	0.101	6.67
7	$V_r = -0.0002(N^*)^2 + 0.0055N^* + 1.3779$	0.2959	0.005	0.35

A comparison of evolution of loss pressure coefficients with N^* is presented at Fig. 8(a). Equations of linear interpolation for loss pressure coefficients K_{volute} are presented at Tab. 12. The loss coefficient decreases with mesh refinement and the turbulence models has different limits (exact values) when $N^* \to 0$. The R^2 varies between 0.7773 at Realizable $k - \epsilon$ model to 0.9828 at SARC model. R^2 values are good (greater than 0.90) to all models except Realizable $k - \epsilon$ and Realizable $k - \epsilon$ with EWE.
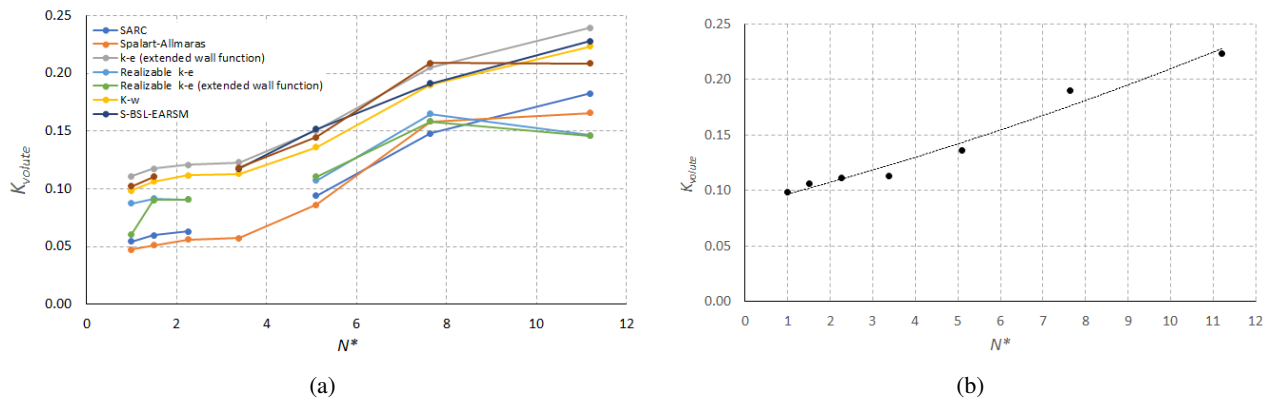

Figure 8: **Variation of loss coefficient pressure with the mesh size: (a) values for all turbulence models and (b) polynomial interpolation for $k - \omega$ model.**

Table 12: **Correlations of loss pressure coefficient K_{volute} for all the turbulence models.**

Turbulence model	Linear equation of k_{volute}	R^2	Error Absolute	Error Rel (%)
1	$K = 0.0131N^* + 0.0374$	0.9828	0.017	45.01
2	$K = 0.0133N^* + 0.0277$	0.9163	0.020	70.68
3	$K = 0.0133N^* + 0.0912$	0.9682	0.020	21.72
4	$K = 0.0072N^* + 0.0801$	0.7773	0.007	9.08
4A	$K = 0.0083N^* + 0.0696$	0.8132	0.009	13.16
5	$K = 0.0128N^* + 0.0812$	0.9701	0.017	21.02
6	$K = 0.0140N^* + 0.0764$	0.9794	0.041	53.50
7	$K = 0.0118N^* + 0.0902$	0.9005	0.012	13.05

At Fig. 9 the residual evolution of continuity equation, momentum equation in x, and turbulence viscosity ν_t or turbulent kinetic energy k and dissipation rate of kinetic energy ϵ are shown for SARC, $k - \epsilon$, Realizable $k - \epsilon$ with EWF and $k - \omega$ models for the more refined mesh, number 8. The convergence, or any model, occurs before iteration 3000. The final results for Realizable $k - \epsilon$ and $k - \omega$ has small oscillation. The label at each curve is the decimal logarithmic value of equation residual. The smaller final residuals occurs for $k - \omega$ at all equations $d = 10^{-6.88}$, $w_x = 10^{-6.39}$, $k = 10^{-7.79}$ and $\epsilon = 10^{-6.68}$, that are very low residuals. Although Realizable $k - \epsilon$ model presents stable residual evolutions, values of residues are greater than for any other model for all the quantities with $d = 10^{-3.26}$, $w_x 10^{-4.26}$, $k = 10^{-3.32}$ and $\epsilon = 10^{-5.88}$. The SARS model presents low residuals for all quantities $d = 10^{-5.36}$, $w_x = 10^{-4.6}$

and $\nu_t = 10^{-8.8}$ despite showing some oscillation in residuals of continuity and velocity equations. Concerning $k - \epsilon$ model the final residuals presents oscillation for all equation, smaller at k and ϵ, with an order of magnitude $10^{\pm 0.04}$; the residuals are $k = 10^{-6.81}$ and $\epsilon = 10^{-7.10}$, respectively. At $k - \epsilon$ model the greatest oscillation is for velocities equations with the residual of $w_x = 10^{-4.85 \pm 0.30}$; for mass equation the residual is $d = w_x = 10^{-3.62 \pm 0.15}$.

(a)

(b)

(c)

(d)
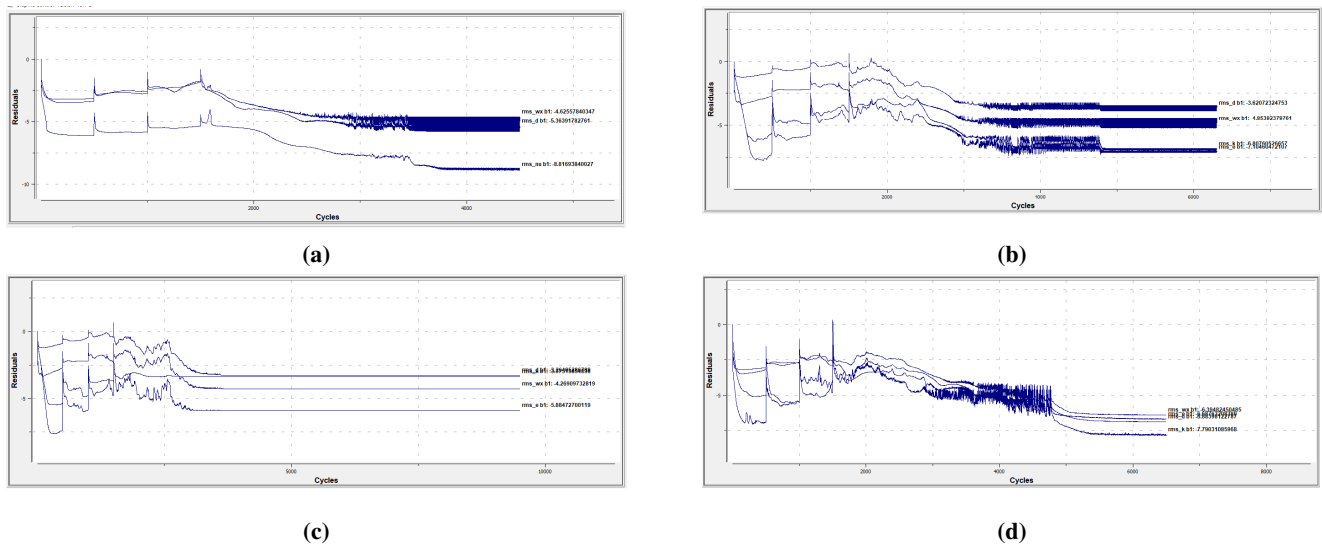
Figure 9: **Evolution of continuity, momentum in x and turbulence quantities for mesh 8: (a) SARC; (b) $k - \epsilon$; (c) Realizable $k - \epsilon$ with extended wall functions and (d) $k - \omega$.**
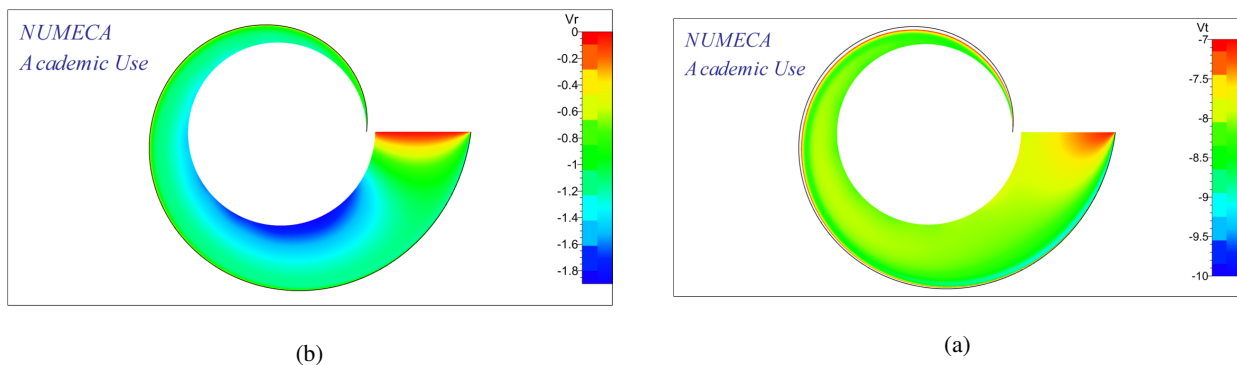

(b)

(a)

Figure 10: **Isolines of radial and tangential velocities components obtained with $k - \omega$ turbulence model for the more refined mesh: (a) radial velocity component V_r and (b) tangential velocity component V_t.**

Isolines for tangential and radial velocities, computed with $k - \omega$ turbulence model for the more refined mesh are presented at Fig. 10. As expected the radial component decreases with radio r. The mean value of V_r for $r = 0.5$ m, the rotor radius, is 1.355 m/s. Figure 10 (a) shows that distribution flow rate is not uniform and that the flow rate is greater for $200° < \theta < 320°$. The value of V_r is very low close inlet section. The isolines of tangential velocity V_t at Fig 10 (b) show that V_t increases with the radius, for $270° < \theta < 360°$, except near the wall, where due no-slip condition $V_t = 0.0$. For small values of θ, V_t distribution becomes close to a free vortex distribution with $rV_t = 4.532$ m^2/s at the inlet section. For $R_a(\theta = 0°) = 0.568$ m the value of V_t for a free vortex distribution must be 7.98 m/s.

4. CONCLUSION

A study of mesh quality and influence of turbulence model on centripetal flow through the two-dimensional volute of a biradial hydraulic turbine is presented. The quality parameters of eight different meshes are analysed and compared. The coarse mesh has 21372 cells and 44422 nodes, and the more refined 130944 cells and 267930 cells. The meshes were generated by HEXPRESS™ code. A geometrical similarity was intended when generating the meshes, multiplying by 1.5 the number of initial mesh cells when they were refined. The similarity of meshes was compromised as the mesh generation is automatic by HEXPRESS™, and to generate the meshes numbers 1 to 3, the number of refinements was 3. At mesh 4, this number was equal to 2. Only mesh 5 to 8 have several refinements equal to 1. On generating the boundary layer mesh, the optimal number of layers suggested by HEXPRESS code was used. The maximum value was 20 at the smaller mesh and the minimum 13 at the more refined mesh.

The first criteria to evaluate mesh quality was the non-existence of negative, concave, related or twisted cells. This criterion was respected for all the meshes studied. A comparison of expansion ratio, aspect ratio, orthogonality, equian-

gular skewness and adjacent volume ratio for all meshes is presented. Criteria to measure quality for those proprieties are presented, and the percentage of elements that are classified (labelled) as not good is calculated and shown. These values are always less than 0,2% for all proprieties, except the adjacent volume ratio and monotonically decrease when the meshes are refined. For the more refined mesh, the referred percentage for all proprieties, except the adjacent volume ratio, is lower than 0.02%.

The centripetal flow was computed for all referred meshes using eight different turbulent models, six linear eddy viscosity models: Spalart-Allmaras, SARC, $k - \epsilon$ with EWF, Realizable $k - \epsilon$ and the Realizable $k - \epsilon$ with EWF, $k - \omega$ (M-SST) and two non-linear eddy viscosity models: S-BSL-EARSM and S-BSL-EARSM with EWF. Correlations are established for mean radial and tangential velocity components, angle $\bar{\alpha}$ at outlet section, and loss coefficient pressure K_{volute} with the dimensionless number N^*. The extrapolated values for an infinity number of cells, $N^* = 0.0$, and absolute and relative error are computed and presented. The error for $\bar{V}_r$, $\bar{V}_t$ and $\bar{\alpha}$ are smaller for $SARC$, $k - \epsilon$ and $k - \omega$ turbulence models.

Residuals of the continuity equation, momentum equation in x, and turbulence viscosity ν_t for the SARC model or k and ϵ for the other models are presented and compared. The convergence occurs before iteration number 3000. For SARC and $k - \epsilon$ model, an oscillation on residual is observed at the end of the iterative procedure. Realizable $k - \epsilon$ with EWF and $k - \omega$ do not show any oscillation. Residuals are smaller for the $k - \omega$ model. $k - \omega$ do not show any oscillation of residuals at the end of the iterative procedure.

Computed distributions of velocities components V_r and V_t show that the flow is not distributed uniformly, with a lower value of flow rate close to the inlet section. Velocity tangential distribution shows that V_t is greater close to the inlet section and that free vortex distribution only is approximately observed for $0 < \theta < \pi/2$.

5. ACKNOWLEDGMENTS

6. REFERENCES

ANSYS, 2016. "ANSYS Fluent - CFD Software | ANSYS". Technical report, ANSYS Inc. URL http://www.ansys.com/products/fluids/ansys-fluent.

Carrelhas, A.A.D., Gato, L.M.C., Henriques, J.C.C. and Falcão, A.F.O., 2020. "Experimental study of a self-rectifying biradial air turbine with fixed guide-vanes arranged into two concentric annular rows". *Energy*, Vol. 198, p. 117211. ISSN 0360-5442. doi:10.1016/j.energy.2020.117211.

de Brederode, V., 1997. *Fundamentos de Aerodinâmica Incompressível*. Author edition, Lisbon, Portugal. 735 p.

Eça, L.M.R.C., 2022. "Number of cells on boundary layer mesh". Private communication, Universidade de Lisboa. Instituto Superior Técnico, Lisbon.

Elmekawy, A.N., 2018. "Global mesh controls. introduction to ansys meshing. module 3.: Global mesh controls". https://drahmednagib.com/courses/cad/lectures, Mechanical Engineering, University of Alexandria, Alexandria,Egypt.

Falcão, A.F.O., Gato, L.M.C. and Nunes, E.P.A.S., 2013a. "A novel self-rectifying air turbines for use in wave energy converters. Part 2. Results from model testing". *Renewable Energy*, Vol. 53, pp. 159–164. ISSN 0960-1481. doi:10.1016/j.renene.2012.11.018.

Falcão, A.F.O., Gato, L.M.C. and Nunes, E., 2013b. "A novel self-rectifying air turbines for use in wave energy converters". *Renewable Energy*, Vol. 50, pp. 289–298. ISSN 0960-1481. doi:10.1016/j.renene.2012.06.050.

Falcão, A.F.O. and Gato, L.M.C., 2011. "Turbine with radial inlet and outlet flow rotor for use in bi-directional flows." Patent no. wo 2011/102746 a2, Instituto Superior Técnico. University of Lisbon.

Falcão, A.F.O. and Henriques, J.C.C., 2016. "Oscillating-water-column wave energy converters and air turbines: A review". *Renewable Energy*, Vol. 85, pp. 1391–1424. ISSN 0960-1481. doi:10.1016/j.renene.2015.07.086.

Falcão, A.F.O., Henriques, J.C. and Gato, L.M.C., 2018. "Self-rectifying air turbines for wave energy conversion: A comparative analysis". *Renewable and Sustainable Energy Reviews*, Vol. 91, pp. 1231–1241. ISSN 1364-0321. doi:10.1016/j.rser.2018.04.019.

Falcão, A.F.O., 2011. *Turbomáquinas*. Associação de Estudantes do Instituto Superior Técnico, Lisbon.

Gato, L.M.C., Carrelhas, A.A.D., Henriques, J.C.C. and Ferreira, D.N., 2021. "Performance improvement fo the biradial self-rectifying biradial air-turbine wfor wave energy conversion by multi-row guide-vanes: Design and experimental results". *Energy*, Vol. 216, p. 119110. ISSN 0360-5442. doi:https://10.1016/j.energy.2020.119110.

George, W.K., 2013. "Lectures in turbulence for the 21st century". Lectures, Imperial College of London, Chalmers University of Technology, Gothenburg, Sweden.

Hakimi, N., 1997. *Preconditioning methods for time dependent Navier-Stokes equations*. Department of Fluid Mechanics,, Brussels, Belgium.

HEXPRESS™, 2021. *User Guide - HEXPRESS™ 11.1*. Cadence, Brussels, Belgium.

Kitano, H., Tokuda, K., Sakagami, T., Tajima, S., Asai, Y., Werth, A., Nishimura, M., Morita, T., Yoshimura, T. and Tokoro, M., 2014. "Open energy systems (oes)". *Japan Solar Energy Society*, Vol. 40, No. 5, pp. 29–31.

Langrty, R.B. and Menter, F.R., 2009. "Correlation-based transition modeling for unstructured parallelized computational fluid dynamics codes". *AIAA Journal*, Vol. 47, No. 12, pp. 2894–2906. doi:10.2514/1.42362.

Launder, B.E. and Spalding, D.B., 1974. "The numerical computation of turbulent flow". *Computer Methods in Applied Mechanics*, Vol. 3, No. 2, pp. 269–289. doi:10.1016/0045-7825(74)90029-2.

M L Shur, M K Strelets, A.K.T. and Spalart, P.R., 2000. "Turbulence modeling in rotating and curved channels: Assessing the spalart-shur correction". *AIAA Journal*, Vol. 38, No. 5, pp. 784–792.

Maduro, A.R., Gato, L.M.C., Henriques, J.C.C. and Ferreira, D.N., 2017. "Design and optimization of fixed guide-vanes arranged into concentric annular rows for a self-rectifying biradial air-turbine". In *Proceedings of the 12th European Wave and Tidal Energy Conference, EWTEC2017*. ABCM, Cork, Ireland, Vol. 1, pp. 1022–1–1022–6.

Mayo, D.C. and Lestriez, R., 2020. "Mesh generation software. some guidelines." http://numiberica.com/en/index.html,(accessed: 09.03.2022), Numeca Ibérica, Spain.

Menter, F.R., 1994. "Two-equation eddy viscosity turbulence models for engineering applications". *AIAA Journal*, Vol. 32, No. 8, pp. 1598–1605. doi:10.2514/3.12149.

NUMECA, 2021. *Theory Guide - FINE/OPEN with OpenLabs 11.1*. Cadence, Brussels, Belgium.

Ocean Energy Europe, 2022. "Powered by the ocean". https://www.oceanenergy-europe.eu/ocean-energy/., OEE.

Panton, R.L., 2001. "Overview of the self-sustaining mechanisms of wall turbulence". *Progress in Aerospace Sciences*, Vol. 37, No. 4, pp. 341–383.

Pfleiderer, C., 1960. *Bombas Centrífugas y Turbocompressor*. Editorial Labor, Barcelona. 632 p.

Pfleiderer, C. and Petermann, H., 1979. *Máquinas de Fluxo*. Livros Técnicos e Científicos, Rio de Janeiro. 480 p.

POINTWISE, 2021. "User manual. Area and volume ratio". https://www.pointwise.com/doc/user-manual/examine/functions/area-volume-ratio.html, Cadence.

SIMSCALE, 2022. "Documentation. Mesh quality". https://www.simscale.com/docs/simulation-setup/meshing/mesh-quality/, SIMSCALE.

Spalart, P.R. and Allmaras, S.R., 1994. "A one equation turbulence model for aerodynamic flows". *La Recherche Aérospatial*, Vol. 1, No. 13, pp. 5–21. doi:10.2514/6.1992-439.

U Goldberg, O.P. and Chakravarthy, S., 1998. "A wall-distance-free $k - \epsilon$ model with enhanced near-wall treatment". *ASME Journal of Fluids Enginnering*, Vol. 120, No. 3, pp. 457–462. doi:10.1115/1.2820684.

Wasserman, S., 2021. "Choosing the right turbulence model for your CFD simulation. turbulence model definitions, strengths, weaknesses and best practices for your CFD simulation". Web page, Engineering.com, https://www.engineering.com/story/choosing-the-right-turbulence-model-for-your-cfd-simulationr.

Yang, Z. and Shih, T.H., 1993. "A k-ϵ model for turbulence and transitional boundary layer". Technical memorandum, NASA Lewis Research Center, Cleveland, USA.

7. RESPONSIBILITY NOTICE

The authors are the only responsible for the printed material included in this paper.